Z. Phys. Chem. **226** (2012) 1125–1147 / **DOI** 10.1524/zpch.2012.0305

Kinetics of Coupled Double Proton and Deuteron Transfer in Hydrogen-Bonded Ribbons of Crystalline Pyrazole-4-carboxylic Acid

By Veronica Torres[1], Juan-Miguel Lopez[1,2], Uwe Langer[1,#], Gerd Buntkowsky[3], Hans-Martin Vieth[4], Jose Elguero[5], and Hans-Heinrich Limbach[1,*]

[1] Institut für Chemie und Biochemie, Freie Universität Berlin, Takustr. 3, 14195 Berlin, Germany
[2] CIC Energigune, Albert Einstein 48, 01510 Miñano (Álava), Spain
[3] Eduard-Zintl-Institut für Anorganische und Physikalische Chemie, Technische Universität Darmstadt, Petersenstr. 20, 64287 Darmstadt, Germany
[4] Institut für Experimentalphysik, Freie Universität Berlin, Arnimallee 14, 14195 Berlin, Germany
[5] Instituto de Química Médica, CSIC, Juan de la Cierva 3, 28006 Madrid, Spain

Dedicated to Professor Hans Wolfgang Spiess on the occasion of his 70th birthday

(Received June 21, 2012; accepted in revised form September 21, 2012)
(Published online October 29, 2012)

Solid State NMR / Hydrogen Bonded Ribbon / Proton Tautomerism / Order-Disorder Transition / Kinetic Hydrogen/Deuterium Isotope Effects / Heavy Atom Motions and Hydrogen Tunneling

The proton tautomerism of pyrazole-4-carboxylic acid (PCA) has been studied by a combination of ^{15}N CPMAS and ^{2}H NMR spectroscopy and relaxometry. Down to 250 K, PCA forms a hydrogen bonded ribbon where adjacent carboxylic and pyrazole groups are linked by an OH···N and an O···HN hydrogen bond, forming either the tautomeric state A or B. Down to about 250 K, the tautomerism is fast on the NMR timescale and degenerate, corresponding to a phase exhibiting dynamic proton disorder. At lower temperatures, a transition to an ordered phase is observed with localized protons, assigned to an all-syn conformation adopting the sequence of tautomeric states ..ABABA.. The longitudinal ^{15}N relaxation times T_1 of PCA-$^{15}N_2$ have been measured at 9.12 MHz (2.1 T). Because of the low field, a chemical shift anisotropy mechanism could be neglected, and the data were analyzed in terms of a dipolar ^{1}H-^{15}N relaxation mechanism, yielding the rate constants k^{HH}. The rate constants k^{HD} and k^{DD} were obtained from the measurement and analysis of the ^{2}H T_1 values of PCA-$^{15}N_1$-$d_{0.9}$ and PCA-$^{15}N_1$-$d_{0.1}$ measured at 46.03 MHz. Within the margin of error, no kinetic isotope effects could be detected, in contrast to previous results reported for the very fast tautomerism of solid benzoic acid dimers and the much slower tautomerism of solid 3,5-diphenyl-4-brompyrazole (DPBrP) dimers. The Arrhenius curves of all three systems were simulated using the Bell–Limbach tunneling model. Evidence for a major heavy atom motion for the tautomerism of PCA is obtained, associated with small angle reorientation of PCA molecules

* Corresponding author. E-mail: limbach@chemie.fu-berlin.de
# *Present address*: Bruker BioSpin GmbH, Silberstreifen 4, 76287 Rheinstetten, Germany

around the molecular axis. The observed proton order-disorder transition and the mechanism of the observed rate process are discussed in terms of a coupling of adjacent tautomeric states.

1. Introduction

Up to date, in contrast to the theory of electron transfer, there is no general accepted theory of hydrogen transfer in condensed matter. As proton transfer is usually coupled to charge transfer, it is not surprising that there has been a special experimental [1–3] and theoretical interest [4–6] in neutral hydrogen transfer reactions, where one H is transferred along a resonance-assisted intramolecular hydrogen bond or where two or more hydrogen atoms are transferred in coupled hydrogen bonds. Of particular interest are (i) solid state measurements by which diffusion of reactants is avoided, and (ii) measurements of kinetic hydrogen/deuterium isotope effects of degenerate hydrogen transfer reactions which provide information about tunneling of the light hydrons (proton, deuteron, triton) and the contribution of heavy atom motions. Such data can be obtained preferentially by solid state NMR line shape analyses for processes on the millisecond [7,8] and by relaxation studies for processes on the micro- to nanosecond time scale. ^{1}H relaxation of static powders is based on the modulation of homonuclear dipolar couplings upon motions of H in hydrogen bonds [9,10]. H jumps from and to nitrogen may not only modulate ^{15}N chemical shifts giving rise to typical line shape changes but also ^{1}H-^{15}N heteronuclear dipolar couplings which may be observed by the measurement of ^{15}N longitudinal relaxation times under magic angle spinning (MAS) conditions and cross polarization (CP) techniques [11]. Most important is, however, deuteron relaxation where jumping deuterons modulate either the quadrupolar interaction or where deuterons are relaxed via the dipole–dipole interaction with jumping protons. The study of ^{2}H relaxation has been made possible by the pioneering work of Spiess *et al.* [12] on Fourier Transform ^{2}H NMR spectroscopy. Kinetic hydrogen/deuterium isotope effects of fast hydron transfers in solids can then preferentially be elucidated by a combination of either ^{1}H and ^{2}H relaxation [13–17], or of ^{15}N and ^{2}H relaxation [18–20].

Some typical examples which have been studied in the past are depicted in Fig. 1. For all cases it has been shown that the hydron transfer proceeds by tunneling, even at room temperature. In the solid state, large kinetic hydrogen/deuterium isotope effects have been observed and analyzed in the case of the tautomerism of N,N′-diphenyl-6-aminofulvene-1-aldimine (Fig. 1a) and of diarylamidine dimers (Fig. 1d), which have been studied by a combination of ^{15}N and ^{2}H relaxometry [21,22]. Multiple proton transfers in solid pyrazole dimers, trimers and tetramers (Fig. 1e to 1g) are slower and have been studied by ^{15}N NMR magnetization transfer and line shape analysis [23–31]. The fastest process in Fig. 1 is the tautomerism of benzoic acid dimers in the solid state, elucidated by ^{1}H and ^{2}H relaxometry [13–15].

Besides the pyrazoles, the gas phase degeneracy of the reactions in Fig. 1 is lifted by solid state interactions which lower the energy of one tautomer and increase the energy of the other one. In solid tropolone (Fig. 1b) only one tautomer is observed as the proton is blocked on one of the two heavy atoms, in contrast to the gas phase where tropolone exhibits tunnel splittings in its vibrational spectra [32]. Spiess *et al.* [33] have shown by two-dimensional rotor-synchronized ^{13}C NMR that a very slow tautomerism

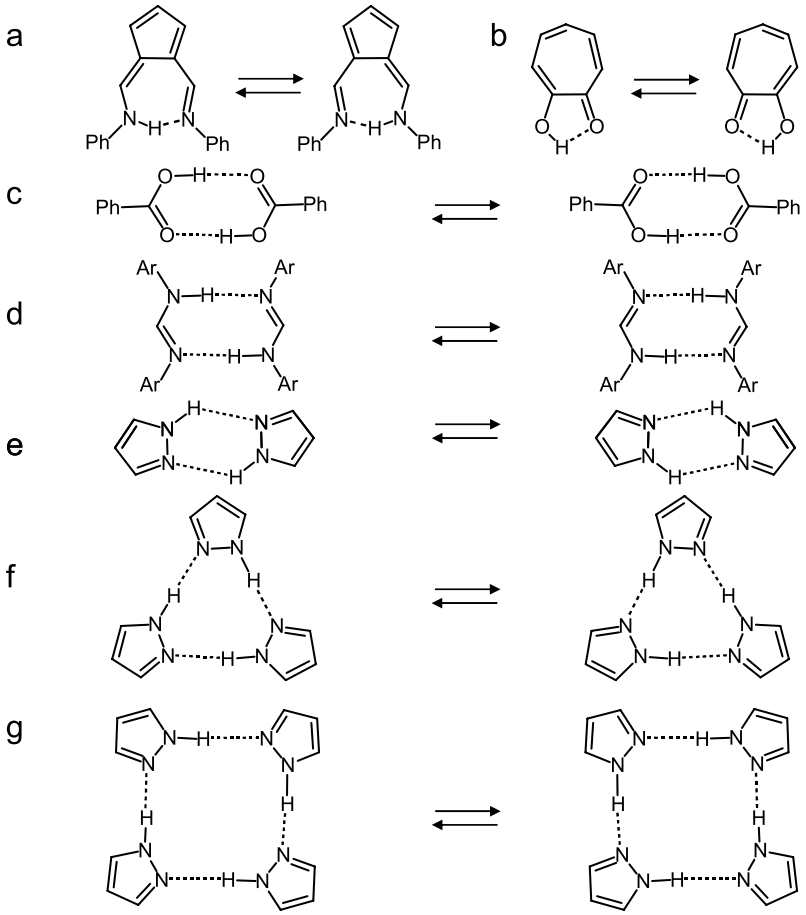

Fig. 1. Hydrogen bonded systems exhibiting multiple proton transfers in the solid state. a N, N′-diphenyl-6-aminofulvene-1-aldimine [19], b tropolone [32,33], c benzoic acid dimer [13–15], d arylamidine dimer [21, 22], e pyrazole dimer, f pyrazole trimer and g pyrazole tetramer [24–30].

of solid tropolone observed by Bax *et al.* [34] is associated with molecular jumps into neighboring vacant molecular sites.

Some years ago some of us have found an intriguing case of coupled proton and heavy atom transfer [35], *i.e.* the case of crystalline pyrazole-4-carboxylic acid (PCA, Fig. 2a). Single crystal X-ray crystallography indicated that the molecule forms linear ribbons linked by double hydrogen bonds between the pyrazole and carboxyl groups (Fig. 2b), exhibiting dynamic or static proton disorder. By ^{15}N CPMAS NMR, a single ^{15}N line was observed at room temperature indicating that the disorder is dynamic, caused by a rapid degenerate proton tautomerism between two tautomers A and B according to Fig. 2c. Interestingly, below 250 K, a new phase appeared exhibiting ordered protons, which became dominant around 200 K. *Ab initio* calculations indicated that the OH···N hydrogen bonds are somewhat shorter than O···HN hydrogen bonds, lead-

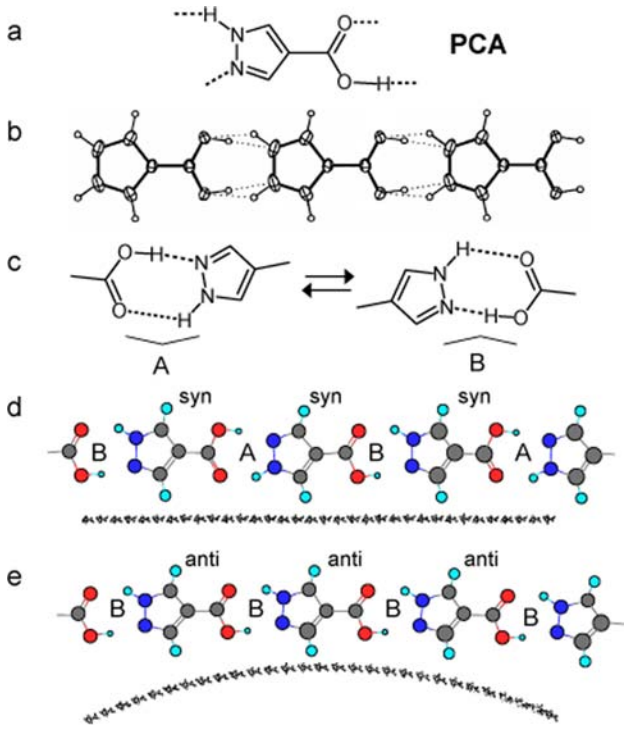

Fig. 2. Structure and properties of hydrogen bonded networks of 1H-pyrazole-4-carboxylic acid (PCA) in the solid state according to Ref. [35]. a Chemical structure of PCA. b X-ray structure of PCA at 295 K. c Solid state tautomerism of PCA between two forms A and B as observed by solid state ^{15}N CPMAS NMR. As OH···N hydrogen bonds are slightly shorter than the O···HN hydrogen bonds, two adjacent PCA molecules form a downward angle in A and an upward angle in B. d Calculated optimized geometries of heptameric units of syn-PCA of the ABABABA type forming an undulated linear ribbon. (e) Calculated optimized geometries of heptameric units of anti-PCA of the BBBBBB type forming a curved ribbon, where about 216 molecules form a circle. Adapted from Ref. [35].

ing to an angle of about 1.7° between two adjacent molecules of the same tautomer type. Thus, it was concluded that a linear ribbon as observed by X-ray crystallography can only be formed in case of a strongly alternating tautomer sequence ...ABABA... as illustrated in Fig. 2d, where the two protons of a given PCA molecule adopt a syn-configuration. By contrast, if all molecules adopt an anti-configuration, *i.e.* when all PCA molecules form the same tautomer -AAAA- or -BBBB- as illustrated in Fig. 2e, a curved ribbon results, where 216 PCA molecules form a circle. This result is schematically illustrated in Fig. 3 which can also explain, that fast crystallization can lead to an amorphous structure with coexisting domains of ordered and disordered protons. It follows, that the PCA molecules must reorient slightly when a double proton transfer according to Fig. 2c occurs. It is then conceivable that such heavy atom motions influence the Arrhenius curve, may reduce the occurrence of tunneling and hence the kinetic hydrogen/deuterium isotope effects which have been found to be large in the case of benzoic acid and pyrazole dimers (Figs. 1c and 1e). Note that the 3,5-dimethyl analogue

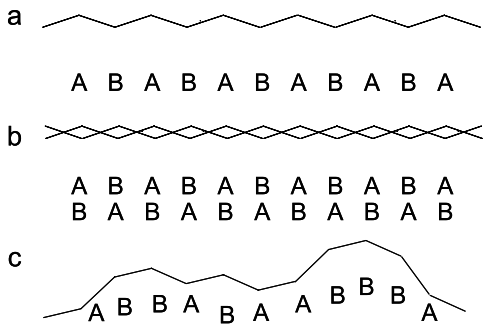

Fig. 3. Schematic structure of undulated linear hydrogen bonded ribbons of PCA in the solid state. a Linear undulated ribbon in the crystalline state at low-temperature exhibiting an alternating sequence of non-equivalent shorter O–H···N and longer O···H–N hydrogen bond pairs (proton order). b Linear ribbon in the crystalline state exhibiting equivalent fast interconverting O–H···N and O···H–N hydrogen bonds at room temperature (proton disorder). c Amorphous PCA formed by fast crystallization exhibiting a non-alternating sequence of O-H···N and O···H–N hydrogen bond pairs. Adapted from Ref. [35].

of pyrazole-4-carboxylic acid also shows fast proton transfer in the solid state according to CPMAS NMR experiments [36].

Therefore, we undertook the present NMR study of polycrystalline PCA in order to characterize the tautomerism of PCA in more detail. After an experimental section, we firstly report the longitudinal ^{15}N relaxation times of PCA which are converted into rate constants using a purely dipolar ^{1}H-^{15}N relaxation mechanism. Kinetic H/D isotope effects are then derived from longitudinal ^{2}H relaxation times at two different deuterium fractions in the mobile proton sites. Finally, the data are discussed in comparison with previous results on pyrazole [1,15] and benzoic acid [31] dimers.

2. Experimental section

2.1 Materials

Pyrazole-4-carboxylic acid-$^{15}N_1$ and -$^{15}N_2$ were synthesized as described previously [35] according to procedures reported in the literature for the unlabeled compounds [37,38], starting from doubly or singly ^{15}N labeled hydrazine sulfate. The latter was synthesized starting from $^{15}NH_3$ and hydroxylamine-O-sulphonic acid [39]. The final product was purified by recrystallization from water, and then dried in vacuum at 60 °C for 24 hours. In order to determine the rate constants of the HD and DD reactions a partially deuterated sample exhibiting a deuterium fraction of $x_D < 0.1$ and a fully deuterated sample with $x_D > 0.9$ were prepared by dissolving PCA under argon atmosphere in a mixture of methanol-d_1 as deuterating agent and the corresponding amount of methanol. The solution was kept at 4 °C overnight under argon atmosphere and the crystals formed were dried in vacuum at 60 °C for 24 hours. To prevent the loss of deuterium during the measurements all the deuterated samples were sealed in 5 mm glass tubes. For the experiments under MAS, Pyrex® inserts for 6 mm MAS rotors purchased from Rototec Spintec GmbH were used. To achieve the necessary symmetry for the

high speed MAS, the filled inserts were mounted in a homebuilt lathe and flame-sealed while spinning.

2.2 NMR spectroscopy

The ^{15}N CPMAS experiments were performed on $^{15}N_2$-PCA at 9.12 MHz and 30.41 MHz using Bruker CXP 100 and MSL 300 NMR spectrometers equipped with standard 7 mm and 5 mm Doty probes. We used a normal cross polarization sequence, which minimizes ringing artifacts [40], with 3 to 8 ms cross polarization times, 6–10 μs ^{1}H-90° pulse width, 3 to 10 s recycle delay. For the measurement of the ^{15}N longitudinal relaxation times T_1 in connection with the CP scheme, a pulse sequence described by Torchia [41] was employed. Due to phase cycling of the first proton 90° pulse and of the receiver phase, at longer equilibration times, the accumulated magnetizations in this experiment cancel; thus, the time dependence of the longitudinal magnetization is given simply by $M = M_o \exp -(t/T_1)$. Between 500 and 2500 scans were accumulated on average, with a contact time for cross polarization of between 1.5 and 5.0 ms, and a repetition time of 1 to 3 s. Low temperature measurements were carried out by passing nitrogen gas through a home built heat exchanger [42] immersed in liquid nitrogen, thus allowing temperatures as low as 90 K to be achieved, maintaining spinning speeds between 2 and 2.5 kHz large enough for obtaining essentially rotational side band-free spectra. The ^{15}N chemical shifts were referenced to external solid $^{15}NH_4Cl$. Sample temperatures were measured using a ^{15}N chemical shift thermometer described previously [43].

The measurements of the ^{2}H T_1 relaxation times were performed using a home-built 7 Tesla spectrometer operating at a Larmor frequency of 46.03 MHz, equipped with a home-built low temperature ^{2}H probe for static samples, and a Chemagnetics probe for samples rotating at the magic angle. Singly ^{15}N labeled PCA – synthesized for another study of [$^{15}N_1$]-4-methylpyrazole – was employed in order to characterize the sample by ^{15}N CPMAS NMR spectroscopy at 30.41 MHz prior to the ^{2}H relaxation time measurements. The latter were determined using a saturation recovery pulse sequence followed by a solid echo sequence. The saturation part involved a string of 90° pulses (3.6 μs) with non-equal spacing to avoid any undesired echo formations. The two 90° pulses of the solid echo sequence were spaced by 35 μs. The echo was recorded and Fourier transformed, allowing the evaluation of T_1 of individual lines in the spectrum. Finally, we note that we did not try to determine the ^{2}H chemical shifts with respect to a standard reference as we did not perform high-resolution ^{2}H MAS measurements. Thus, the frequency of the ^{2}H NMR signal center was set to zero.

3. Results

3.1 ^{15}N spectra and corresponding longitudinal relaxation times

Figure 4a depicts the variable temperature ^{15}N CPMAS NMR spectra of PCA-$^{15}N_2$ which have been described previously [35]. For comparison, we depict in Fig. 4b spectra of PCA-$^{15}N_1$ measured at 30.41 MHz. As discussed above, down to 250 K only a single line at 203 ppm is observed indicating a rapid degenerate proton tautomerism according

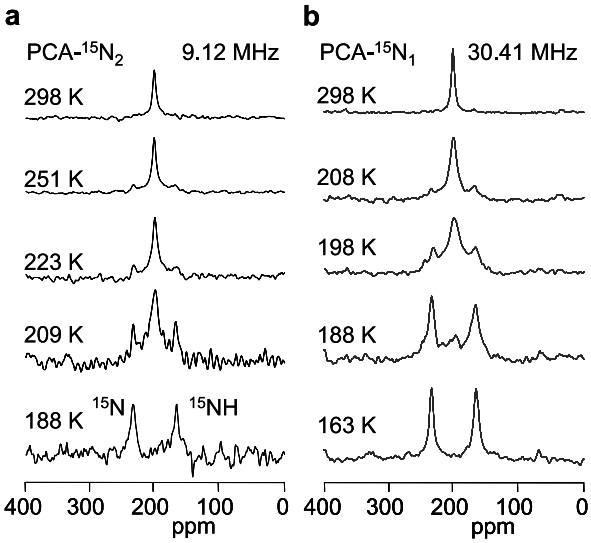

Fig. 4. a 9.12 MHz ^{15}N CPMAS spectra of PCA-$^{15}N_2$ and **b** 30.41 MHz ^{15}N CPMAS spectra of PCA-$^{15}N_1$ as a function of temperature. At room temperature, a single ^{15}N line is observed indicating a fast proton tautomerism according to Fig. 2c. Around 200 K, a disorder-order phase transition is observed leading to proton order. The spectra in **a** are adapted from Ref. [35]. For further explanation see text.

to Fig. 2c, exhibiting an equilibrium constant of $K = 1$. This indicates that the proton disorder observed by crystallography (Fig. 2b) is dynamic. By contrast, below 250 K, two outer lines appear at 233 ppm and 172.5 ppm. Their intensities grow when temperature is further decreased. A variation of cross polarization times did not change this result. Thus, the temperature effects are real and not caused by a temperature-dependent cross-polarization efficiency. The high-field line stems from the protonated and the low-field line from the non-protonated nitrogen atoms of the pyrazole units. At 190 K only the outer signals are observed. This behavior does not follow the usual pattern of decoalescence but indicates a proton disorder-order transition [35].

As noted before [35], freshly prepared PCA often exhibits a ^{15}N line trio similar to the 209 K spectrum in Fig. 4a already at room temperature. The outer signals disappear when the sample is annealed at 150 °C. This observation has been explained in terms of a conversion of a sample exhibiting a structure such as illustrated in Fig. 3c into the linear undulated ribbon structure of Fig. 3a. A comparison of the spectra in Fig. 4a and 4b, for example at 209 K and 208 K, indicates that depending on the exact sample history, the observed proton disorder-order transition can take place at slightly different temperatures.

The proton transfer modulates the ^{1}H-^{15}N dipolar interactions symbolized by double arrows as illustrated at the top of Fig. 6. α represents the jump angle. Thus, ^{15}N relaxometry can be used to obtain the corresponding rate constants [11]. Therefore, we measured the temperature dependent ^{15}N-T_1 relaxation times at 9.12 MHz for the coalesced center line between 373 K and 240 K. We did not measure the relaxation times at 30.41 MHz because at this Larmor frequency ^{15}N relaxation is no longer

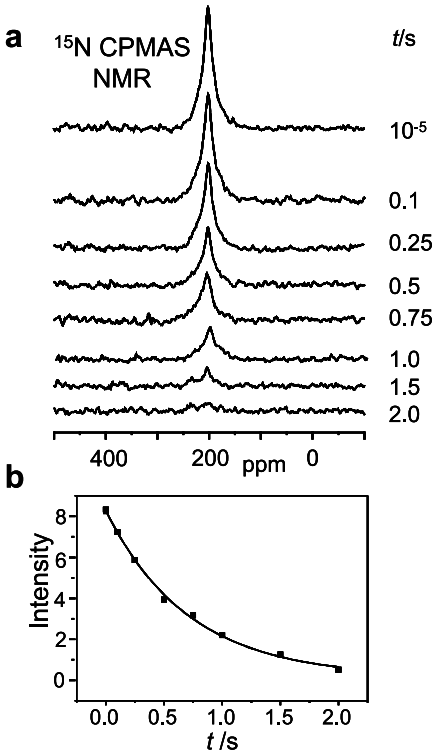

Fig. 5. a ^{15}N-spin lattice relaxation experiment at room temperature for $^{15}N_1$-PCA. **b** Monoexponential fit of the longitudinal magnetization as a function of time.

Table 1. ^{15}N T_1 times measured at 9.1 MHz for ($^{15}N_1$)-1H-pyrazole-4-carboxylic acid and the corresponding calculated rate constants.

T/K	^{15}N T_1/s	$k^{HH} \times 10^{-6}/s^{-1}$	T/K	^{15}N T_1/s	$k^{HH} \times 10^{-6}/s^{-1}$
373	1.45	293	288	0.56	–
358	1.25	205	283	0.67	55
343	1.24	197	273	0.59	36
323	0.99	121	268	0.63	19
310	0.93	105	263	0.63	19
300	0.73	64.5	258	0.71	15
296	0.74	68	240	0.88	11
293	0.71	63			

purely dipolar but contributions from a chemical shielding anisotropy complicate the analysis [11]. As illustrated in Fig. 5, the ^{15}N polarization created by cross polarization decays in a mono-exponential way to zero, as the add-substract scheme used together with alternating $+\pi/2$ and $-\pi/2$ ^{1}H pulses cancel the equilibrium polarizations.

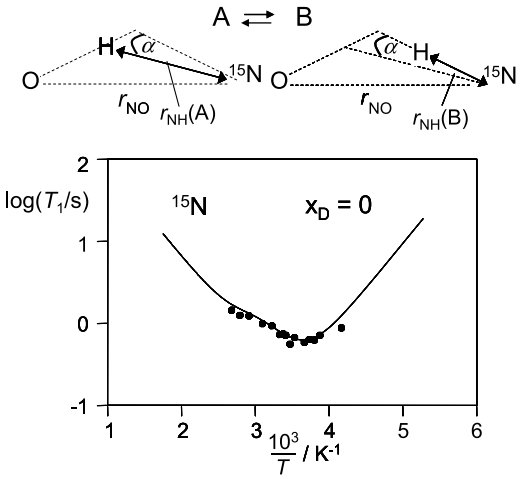

Fig. 6. Longitudinal ^{15}N relaxation times of PCA obtained under CPMAS conditions at a frequency of 9.12 MHz as a function of the inverse temperature. The ^{1}H-^{15}N dipolar interaction modulated by the tautomerism is illustrated at the top. The solid line was calculated as described in the text.

The results of the relaxation experiments are assembled in Table 1 and are plotted in Fig. 6 in a logarithmic way as a function of the inverse temperature. A T_1 minimum of 0.585 s was observed at 273 K. The solid curve was calculated as previously for related cases [11,19,20] using the master equation for the spin–lattice relaxation rates of nuclei S caused by fluctuations of the heteronuclear dipolar interaction with spins I which exchange between two sites [44]. For polycrystalline solids, this equation depends on the molecular orientation with respect to the external magnetic field. However, under MAS conditions, in the presence of a two-state tautomeric equilibrium between two forms A and B, the T_1 values are given in very good approximation by the isotropic average [11]. For a degenerate tautomerism from and to ^{15}N, *i.e.* a tautomerism exhibiting an equilibrium constant of 1, the ^{15}N relaxation rate can then be expressed as

$$\frac{1}{T_{1N}} = \frac{1}{40}\left(\frac{\mu_o}{4\pi}\right)^2 \gamma_N^2 \gamma_H^2 \hbar^2 R \times \left[\frac{\tau_c}{1+(\omega_H-\omega_N)^2\tau_c^2} + \frac{3\tau_c}{1+\omega_N^2\tau_c^2} + \frac{6\tau_c}{1+4(\omega_H+\omega_N)^2\tau_c^2}\right]. \quad (1)$$

$\mu_o = 4\pi 10^{-7}\ \mathrm{V^2s^2/Jm}$ represents the permeability of the vacuum, γ_N and γ_H the gyromagnetic ratios of ^{15}N and of ^{1}H, ω_N and ω_H the corresponding Larmor angular frequencies and $\hbar$ Planck's constant divided by 2π. The inverse correlation time of the degenerate tautomerism is given by

$$\frac{1}{\tau_c} = k_{AB} + k_{BA} = 2k\,, \quad (2)$$

where $k_{AB} = k_{BA} = k$ represent the rate constant of the forward and backward reaction of the degenerate tautomerism. The dipolar interaction between the two spins, modulated

by the tautomerism as illustrated at the top of Fig. 6, leads to the geometric factor

$$R = r_{\mathrm{NH}}^{-6}(\mathrm{A}) + r_{\mathrm{NH}}^{-6}(\mathrm{B}) + r_{\mathrm{NH}}^{-3}(\mathrm{A}) r_{\mathrm{NH}}^{-3}(\mathrm{B})(1 - 3\cos^2\alpha)\,, \tag{3}$$

where $r_{\mathrm{NH}}(\mathrm{A})$ and $r_{\mathrm{NH}}(\mathrm{B})$ represent the NH distances in forms A and B, and α the jump angle as defined in Fig. 6. Note that R should not be confused with the gas constant, used in this work in the context of the Arrhenius equation. In good approximation, one can assume that

$$R = r_{\mathrm{N\ldots H}}^{-6} + r_{\mathrm{NH}}^{-6} + r_{\mathrm{N\ldots H}}^{-3} r_{\mathrm{NH}}^{-3}(1 - 3\cos^2\alpha)\,, \tag{4}$$

where $r_{\mathrm{N\ldots H}}$ represents the long N…H distance and r_{NH} the short NH distance of a given tautomer. The pre-factor in Eq. (1) is given for a ^{1}H-^{15}N spin pair by 1.4605×10^{-8} [s^{-2}Å^6].

The solid curve in Fig. 6 was obtained assuming an Arrhenius law $k_{\mathrm{AB}}^{\mathrm{HH}} = k^{\mathrm{HH}} = A\exp(-E_{\mathrm{a}}^{\mathrm{HH}}/RT)$ in the temperature range where the experimental data could be obtained. Fixed parameters of the least-squares fitting procedure were the Larmor frequencies $\nu_{\mathrm{H}} = 90.02$ MHz and $\nu_{\mathrm{N}} = 9.12$ MHz, and variable parameters were the geometrical factor R, the effective pre-exponential factor A and the activation energy $E_{\mathrm{a}}^{\mathrm{HH}}$. We obtained the values $R = 0.4$ Å^{-6}, $E_{\mathrm{a}}^{\mathrm{HH}} = 21$ kJ mol^{-1} and $A = 3 \times 10^{11}$ s^{-1}, valid between 240 K and 380 K. Using Eq. (1) and the value of R obtained the ^{15}N-T_1 values were finally converted into the rate constants included in Table 1.

Generally, it is difficult to derive exact dipolar couplings from the geometric factor R, because of the two unkowns, $r_{\mathrm{N\ldots H}}$ and α in Eq. (4). For $r_{\mathrm{N\ldots H}} \gg r_{\mathrm{NH}}$ the upper value of $r_{\mathrm{NH}} = 1.16$ Å results which is lowered if $r_{\mathrm{N\ldots H}}$ is increased. Thus, the value of R is compatible with the value of 1.05 Å expected from OHN hydrogen bond correlations [45,46] for an N…O distance of 2.76 Å [35].

3.2 ^{2}H NMR solid-echo spectra and corresponding longitudinal relaxation times

In order to obtain information about the rate constants $k_{\mathrm{AB}}^{\mathrm{HD}}$ and $k_{\mathrm{AB}}^{\mathrm{DD}}$ we performed ^{2}H-T_1 measurements on PCA. As the ^{2}H-^{15}N dipolar interactions are small only the quadrupolar ^{2}H interaction needs to be taken into account in the analysis of the relaxation times.

In a first step, in order to determine the strength of the ^{2}H-quadrupolar interaction, solid-echo experiments were performed at 150 K and 293 K on samples of PCA at deuterium fractions of $x_{\mathrm{D}} > 0.9$ and < 0.1 in the mobile proton sites. Some results are included in Fig. 7. At 150 K and $x_{\mathrm{D}} > 0.9$, for the phase with ordered protons, the signal could be simulated assuming the presence of two non-exchanging deuteron sites I and II, exhibiting different quadrupole coupling constants $Q_{zz}(\mathrm{I}) = 134$ kHz, *i.e.* $Q_{cc}(\mathrm{I}) = 4/3\,Q_{zz}(\mathrm{I}) = 179$ kHz and $Q_{zz}(\mathrm{II}) = 103$ kHz, *i.e.* $Q_{cc}(\mathrm{II}) = 137$ kHz. Within the margin of error the corresponding asymmetry factors were the same for both sites, *i.e.* $\eta = 0$. We tentatively assign I to the OD and II to the ND deuterons because quadrupole coupling constants of OD groups [47,48] are on average larger than those of ND groups [49].

The spectra at 293 K were simulated using the values $Q_{zz} = 116$ kHz, *i.e.* $Q_{cc} = 155$ kHz and $\eta = 0.2$, indicating fast exchange of the deuterons between oxygen and nitrogen. Unfortunately, we were not able to calculate the room temperature spectra for

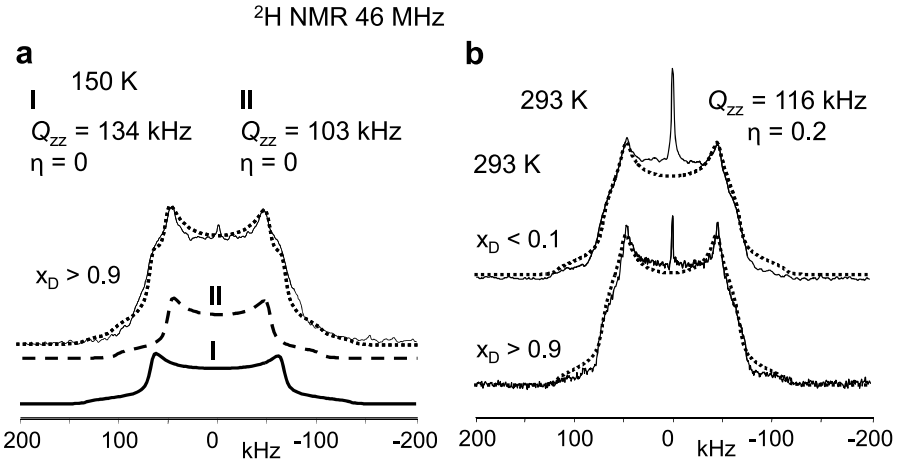

Fig. 7. Superimposed experimental and calculated ^{2}H solid-echo NMR spectra at 46 MHz of PCA. **a** Fully deuterated sample ($x_D > 0.9$) at 150 K. **b** Fully and partially ($x_D < 0.1$) deuterated samples at 293 K. For further explanation see text.

a degenerate tautomerism using the low-temperature parameters in order to determine the deuteron jump angle. For this task, the chemical shift difference of OD and ND deuterons needs to be taken into account which requires careful low-temperature MAS measurements.

In the second step, the longitudinal ^{2}H relaxation times T_1 were measured for both samples between 403 K and 210 K. Experiments at room temperature and below were carried out on static samples, whereas at higher temperatures measurements were performed on samples spinning at the magic angle with a spinning speed of 5 kHz. At all temperatures the signals grow exponentially with time. An example of the static experiment is shown in Fig. 8. The T_1 times obtained for both samples are listed in Tables 2 and 3, and are plotted in a logarithmic way as a function of the inverse temperature in Fig. 9.

In order to calculate the solid line in Fig. 9 we used the master equation for the longitudinal relaxation of deuterons in a hydrogen bond in the presence of a degenerate tautomerism [50]

$$\frac{1}{T_{1\mathrm{I}}} = \frac{3\pi^2}{10}\frac{C}{4}\left(\frac{\tau_\mathrm{c}}{1+\omega_\mathrm{I}^2\tau_\mathrm{c}^2} + \frac{4\tau_\mathrm{c}}{1+4\omega_\mathrm{I}^2\tau_\mathrm{c}^2}\right), \tag{5}$$

where

$$C = \left(\frac{\mu_\mathrm{o}}{4\pi}\right)^2\left(1+\frac{\eta^2}{3}\right)\left(q_{\mathrm{cc}}\,(\mathrm{A})^2 + q_{\mathrm{cc}}\,(\mathrm{B})^2 - q_{\mathrm{cc}}\,(\mathrm{A})\,q_{\mathrm{cc}}\,(\mathrm{B})\left(3\cos^2\theta - 1\right)\right). \tag{6}$$

Here, the symbols have similar meanings as in Eq. (1). C in s^{-2} is a constant which depends on the quadrupole coupling constants $q_{\mathrm{cc}}(\mathrm{A})$ and $q_{\mathrm{cc}}(\mathrm{B})$ in the two tautomeric states, on the asymmetry factor η and on the jump angle θ between both tensors as illustrated at the top of Fig. 9. However, as noted before [13,19], it is difficult to calculate C

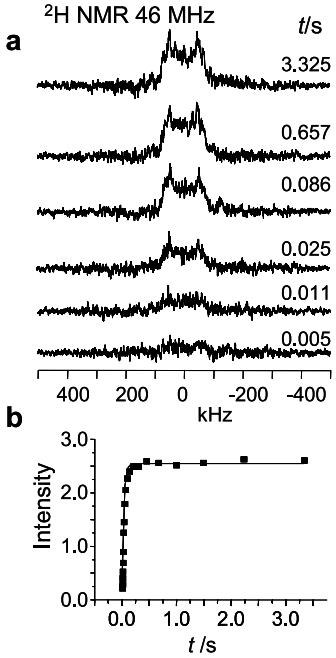

Fig. 8. a Measurement of the ^{2}H longitudinal relaxation times of a static powdered sample of PCA at room temperature, $x_D > 0.9$, 46.03 MHz using the saturation recovery technique. **b** Monoexponential fit of the saturation recovery.

Table 2. ^{2}H T_1 longitudinal relaxation times of solid PCA measured at 46 MHz at a deuterium fraction of $x_D > 0.9$ and corresponding rate constants k^{DD} of DD transfer.

T/K	^{2}H T_1/s	$k^{DD} \times 10^{-6}/s^{-1}$	T/K	^{2}H T_1/s	$k^{DD} \times 10^{-6}/s^{-1}$
403	0.0172	–	275	0.124	15
373	0.0147	–	273	0.0673	27
373	0.0151	–	273	0.0750	24
330	0.0248	87	270	0.156	11
323	0.0246	89	263	0.0803	23
323	0.0230	98	263	0.112	16
323	0.0234	95	260	0.119	15
320	0.0369	44	253	0.0921	19
310	0.0364	52	253	0.118	15
310	0.0451	41	250	0.164	11
298	0.0330	60	250	0.181	10
293	0.0458	41	243	0.169	11
293	0.0347	56	240	0.394	4.5
293	0.0386	50	233	0.498	3.6
293	0.0579	32	230	0.423	4.1
288	0.0506	36	220	0.720	2.4
283	0.0463	40	210	1.013	1.7

Table 3. ^{2}H T_1 longitudinal relaxation times of solid PCA measured at 46 MHz at a deuterium fraction of $x_D < 0.1$ and corresponding rate constants k^{HD} of HD transfer.

T/K	^{2}H T_1/s	$k^{HD} \times 10^{-6}/s^{-1}$	T/K	^{2}H T_1/s	$k^{HD} \times 10^{-6}/s^{-1}$
323	0.019	145	288	0.029	74
320	0.019	151	270	0.105	17
303	0.018	166	250	0.111	16
298	0.026	81	240	0.246	7
293	0.022	94	210	0.493	3.5

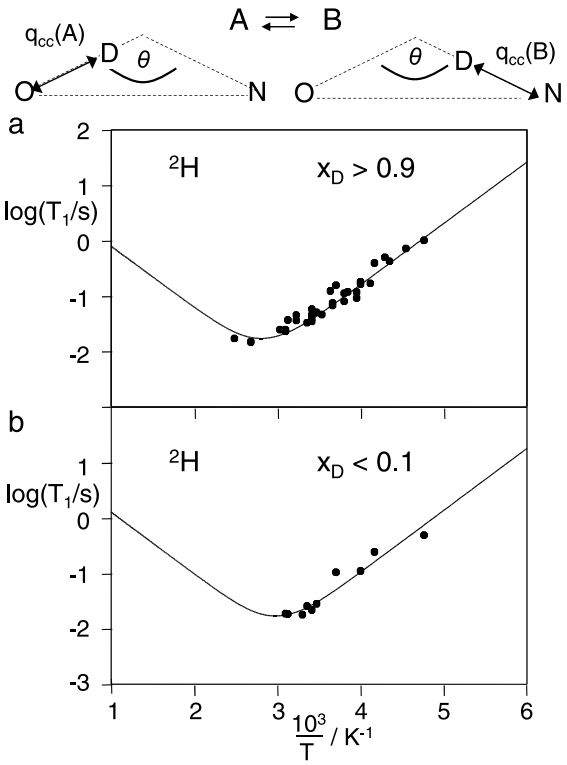

Fig. 9. Longitudinal ^{2}H relaxation times of PCA at $x_D > 0.9$ a and $x_D < 0.1$ b and a frequency of 46.02 MHz as a function of the inverse temperature. The ^{2}H quadrupolar interaction modulated by the tautomerism is illustrated at the top. The solid lines were calculated as described in the text. Because of the smaller deuterium content, fewer data points could be obtained for the sample with $x_D < 0.1$.

from the ^{2}H NMR spectra. Therefore, in a similar way as the factor R in Eq. (1), C was treated as a parameter to be determined by the fit of the experimental data to Eq. (5). A possible temperature dependence of C because of temperature-dependent quadrupole coupling constants as observed for carboxylic acids [51] was neglected. Again, an Arrhenius behavior was assumed in order to describe the dependence of the rate constants

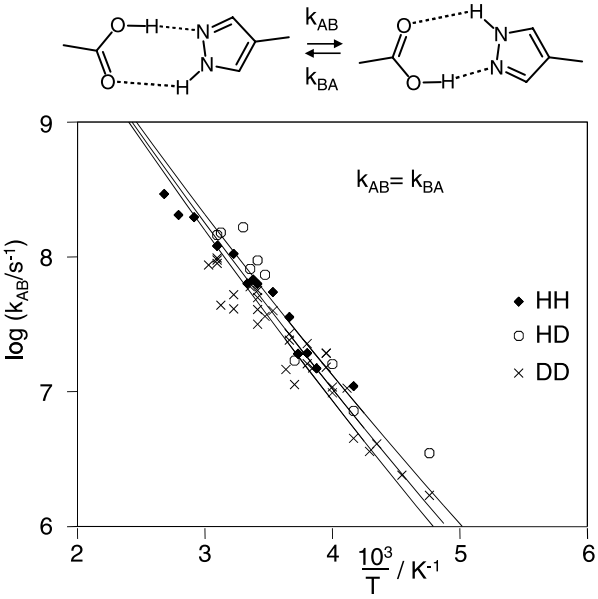

Fig. 10. Arrhenius diagram of the double proton and deuteron transfer in crystalline PCA.

(Eq. 2) of the deuteron tautomerism as a function of temperature. We assumed that the correlation times obtained at $x_D > 0.9$ yield the rate constants $k_{AB}^{DD} = A\exp(-E_a^{DD}/RT)$ and those obtained at $x_D < 0.1$ the rate constants $k_{AB}^{HD} = A\exp(-E_a^{HD}/RT)$. Using Eq. (5) and the values $C = 1.6 \times 10^{10}\,s^{-2}$, $A = 3 \times 10^{11}\,s^{-1}$, $E_a^{DD} = 21.4\,kJ\,mol^{-1}$ and $E_a^{HD} = 21.1\,kJ\,mol^{-1}$ we obtained the solid lines in Fig. 9a and 9b. Again, using the value of C and Eq. (5), we converted the T_1 values into the rate constants k_{AB}^{DD} and k_{AB}^{HD}, included in Tables 2 and 3. Using the parameters obtained by line shape analysis, we find that the value of C is compatible with a jump angle of about 152°.

4. Discussion

The rate constants $k_{AB}^{HH} = k^{HH}$, $k_{AB}^{HD} = k^{HD}$ and $k_{AB}^{DD} = k^{DD}$ obtained for the tautomerism of solid PCA (Fig. 2c) in the high-temperature phase exhibiting hydron disorder, assembled in Tables 1 to 3, are visualized in the Arrhenius diagram of Fig. 10. The rate constants k^{HH} are only slightly larger than those of k^{DD}, whereas the values of k^{HD} exhibit a substantial scattering. Thus, within the margin of error of our measurements, the kinetic HH/HD, HD/DD and HH/DD isotope effects are less than 1.5.

In order to rationalize these findings, let us compare them in Fig. 11 with those obtained previously for the solid benzoic acid dimer and 3,5-diphenyl-4-brompyrazole (DPBrP) dimers. Whereas DPBrP exhibits in the solid state a tautomerism which is degenerate within the margin of error [31], one of the two tautomers of the benzoic acid dimer is preferred in the solid state, *i.e.*, the equilibrium constants of the tautomerism are slightly smaller than unity [9,13–15]. Thus, in this case we have plotted in Fig. 11

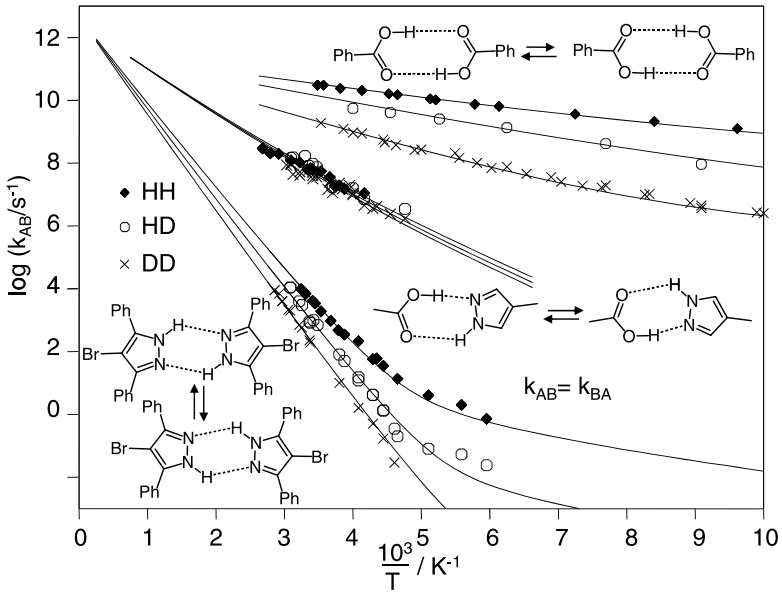

Fig. 11. Comparison of the Arrhenius diagrams of the double proton and deuteron transfers in benzoic acid dimers [1,15], 2,4-diphenyl-3-brompyrazole dimers [31] and crystalline PCA.

the forward rate constants k_{AB}^{LL}, LL = HH, HD, DD according to the analysis presented in Ref. [1].

As has been discussed before [1], proton transfers in NHN hydrogen bonds are often slower than in OHO hydrogen bonds, in agreement with the observation that the heavy atom distances in the latter are shorter and hence the barriers lower than in NHN hydrogen bonds. It is, therefore, not surprising that an intermediate situation is observed in the case of PCA where a carboxylic acid is hydrogen bonded to a pyrazole moiety. However, even more striking is that the double proton transfers of both benzoic acid dimer and of DPBrP are characterized by large kinetic HH/HD/DD isotope effects, whereas the corresponding process in PCA does not exhibit large effects.

In the following discussion we want to address the question of how the order-disorder transition in PCA occurs, and what the mechanism of the double proton transfer is. Two possibilities are illustrated in Fig. 12, *i.e.* a concerted transfer as discussed for the benzoic acid dimer and for DPBrP and a stepwise transfer, as discussed for a variety of intramolecular transfers [1–3].

4.1 Calculation of Arrhenius curves using the Bell–Limbach tunneling model

In order to elucidate what can be learned from the Arrhenius curves of Figs. 10 and 11 we have simulated the Arrhenius curves in Fig. 11 using the Bell–Limbach tunneling model and the parameters assembled in Table 4. This model has been applied to a number of single and multiple proton transfers, mostly degenerate ones, and has been reviewed recently in detail [1–3]. In the context of this study, we will discuss only

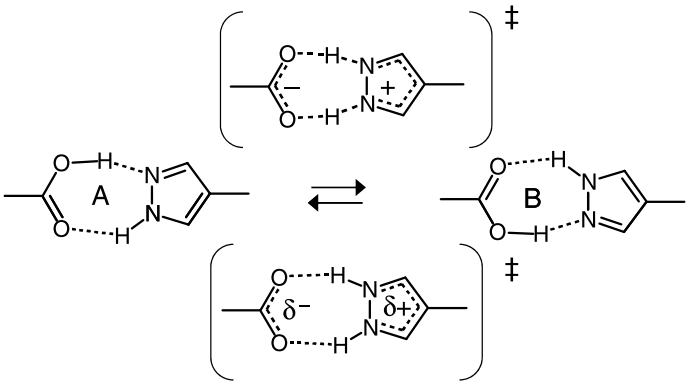

Fig. 12. Concerted *vs.* stepwise double proton transfer between two hydrogen bonded molecules of PCA.

shortly the main tunnel parameters for some typical cases which will assist us later to interpret the results of Fig. 11.

In Fig. 13a and 13b are depicted schematically arbitrary reaction profiles of degenerate single H transfer processes. It is assumed that starting in the initial state, first heavy atom motions are required before the pre-tunneling state is reached, symbolized by a dagger. Naturally, hydrons bound to the heavy atoms move together with the latter. To reach the pre-tunneling state a minimum energy E_m is required which shows little changes upon H/D substitution. Only the energies of the reactant and the pre-tunneling state are depicted as horizontal lines linked by upward curved vertical ones, but not the reaction profiles for these heavy atom motions. This profile can be omitted as it is assumed that the heavy atom motion does not constitute the rate-limiting step. Once the system is in the pre-tunneling state, it is assumed that the reaction profile can be described in terms of an inverted parabolic barrier. The barrier width $2a$ at the base shows little hydron dependence, whereas the barrier heights E_d^H and E_d^D can be different because of losses of zero-point energies in the transition state. The hatched area under the barrier determines the tunneling probabilities. Whereas in Fig. 13a E_m is small and E_d is large, the contrary is assumed in Fig. 13b. The tunneling probabilities also depend strongly on the tunneling mass $m_{eff}^L = m^L + \Delta m$, L = H, D. Δm constitutes an extra term which takes care of heavy atom motions *during* the tunneling process. Such motions arise typically from small displacements of C or N associated with single-double bond distance changes accompanying the hydron transfer.

The corresponding Arrhenius curves of H and D transfer exhibit patterns as illustrated in Fig. 13c and 13d. At high temperatures, the slopes are given by the sums $E_m + E_d^H$ and $E_m + E_d^D$ as illustrated by the dashed Arrhenius curves [1–3]. The kinetic H/D isotope effects are then determined by the difference $E_d^D - E_d^H$. Naturally, if E_d^D and E_d^H are large the difference is also large. Therefore, at high temperature, larger H/D kinetic isotope effects are expected for the profile in Fig. 13a than for the one in Fig. 13b. At low temperatures, the slopes of the Arrhenius curves are given by E_m, leading to parallel Arrhenius curves for H and D. The rate constants are given by the tunnel probabilities in the pre-tunneling state. These constants as well as the kinetic H/D isotope effects at low temperatures depend on all barrier parameters. As illustrated in Fig. 13d, they

Table 4. Rate constants, kinetic isotope effects and Bell–Limbach tunnel parameters of the double hydron transfer in crystalline benzoic acid dimer, diphenylbrompyrazole (DPBrP) dimer and PCA chains.

System	Ref.	LL	$(k^{LL})_{298\,K}/s^{-1}$	$KIE_{298\,K}$	$\log(A/s^{-1})$	E_m	E_d	$E_m + E_d$	Δm/a.m.u.	$2a$/Å
$(PhCOOH)_2$ solid state		HH	9×10^{10}	$k^{HH}/k^{HD} \approx 2.4$	11.6	0.84	5.4	6.2	1.8	0.48
(PhCOOH/PhCOOD) solid state	[17]	HD		$k^{HD}/k^{DD} \approx 6$	11.6	0.84	7.5	8.3	1.8	0.52
$(PhCOOD)_2$ solid state		DD		$k^{HH}/k^{DD} \approx 14$	11.6	1.0	12.1	13	1.8	0.44
		HH	6.5×10^3	$k^{HH}/k^{HD} \approx 5$	12.65	5.6	47.5	53	2.3	0.55
DPBrP crystal	[31]	HD		$k^{HD}/k^{DD} \approx 5$	12.65	5.6	51.1	56.7	2.3	0.55
		DD		$k^{HH}/k^{DD} \approx 25$	12.65	5.6	54.5	60.1	2.3	0.55
		HH	$\approx 6.5 \times 10^6$	$k^{HH}/k^{HD} \approx 1.2$	12.5	17	12.0	29	4	0.2
PCA	this work	HD		$k^{HD}/k^{DD} \approx 1.2$	12.5	17	12.2	29.2	4	0.2
		DD		$k^{HH}/k^{DD} \approx 1.4$	12.5	17	12.4	29.4	4	0.2

E_m, E_d in $kJmol^{-1}$. For explanation of symbols see text.

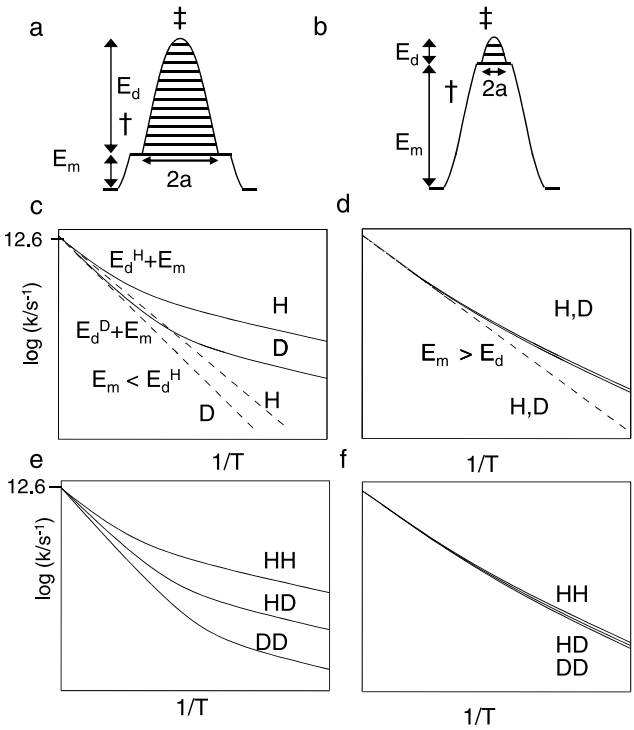

Fig. 13. Reaction profiles a and b and calculated Arrhenius curves of degenerate H c and e and concerted HH d and f transfers using the Bell–Limbach tunneling model. For further information see text.

are especially small for the reaction profile of Fig. 13b. In the intermediate temperature range, the Arrhenius curves exhibit a concave curvature, even in the case of the profile of Fig. 13b.

Similar results are obtained for concerted degenerate double HH transfers as illustrated in Fig. 13e and 13f. If the energy differences $E_d^{DD} - E_d^{HD}$ and $E_d^{HD} - E_d^{HH}$ are similar, two large HH/HD and HD/DD isotope effects are observed in the whole temperature range. At high as well as at low temperatures the rule of the geometric mean is fulfilled, *i.e.* k^{HH}/k^{HD} and k^{HD}/k^{DD} are similar as illustrated in Fig. 13e. Deviations from this rule are observed in the intermediate temperature range, where $k^{HH}/k^{HD} > k^{HD}/k^{DD}$. By contrast, for the profile of Fig. 13f, the Arrhenius curves show again curvature because of a small tunneling contribution, but little kinetic isotope effects.

In Fig. 14a we consider the reaction profile of a degenerate stepwise double hydron transfer where $E_d^L > E_m$. In the case of the HH and DD transfers, both in the first as well as in the second step the same isotope is transferred. Internal return to the reactant state cuts the total rate in half. If the barrier is isotope-dependent, kinetic HH/DD isotope effects result. By contrast, in the case of the HD reaction, only the step in which D is transferred is rate-limiting. Therefore, the HD rates are approximately doubled as compared to the DD rates as illustrated in Fig. 14c [1,52]. Otherwise, the Arrhenius curves behave in the same way as for the single H transfer case depicted in Fig. 13c.

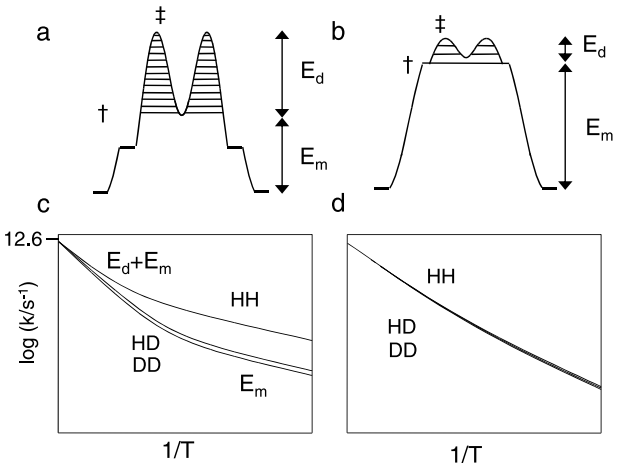

Fig. 14. Reaction profiles a and b and calculated Arrhenius curves of degenerate stepwise HH transfers c and d using the Bell–Limbach tunneling model. For further information see text.

When $E_d^L < E_m$, for a profile such as illustrated in Fig. 14b, again the kinetic isotope effects are drastically reduced although the Arrhenius curves may show still some curvature as depicted in Fig. 14d. Thus, in this case it becomes difficult to distinguish between a concerted and a stepwise transfer. We also note that the concerted and the stepwise HH transfer constitute limiting cases and that various intermediate cases are possible. Rauhut *et al.* [53] have studied "plateau" reactions which are realized when the energy of the intermediate is raised producing a very wide flat single barrier region which cannot be described in terms of an inverted parabola.

Finally, we want to mention that kinetic hydrogen/deuterium isotope effects might be different for non-degenerate transfers as has been discussed previously [1,54].

4.2 Heavy atom motions associated with the double proton transfer of PCA and related systems

Let us have again a look at the Arrhenius curves of Fig. 11 and their parameters included in Table 4. Firstly we note that the total barrier $E_m + E_d$ of the double proton transfer in PCA is close to the arithmetic mean of the corresponding values of benzoic acid dimer and of DPBrP, and hence the rate constants are close to the geometric mean. The main difference is, however, the behavior of the kinetic isotope effects. The double proton transfers in benzoic acid dimer and DPBrP are of the type depicted in Fig. 13e, typical for a concerted reaction mechanism. The minimum energy E_m for tunneling to occur is small in the case of benzoic acid dimer, and mainly caused by the small energy difference between the two tautomers. Below this energy, tunneling can not occur. Apparently, hydrogen bond compression is not necessary to reach the pre-tunneling state. The kinetic HD/DD isotope effects are somewhat larger than the HH/DD isotope effects, a finding which has been assigned to a weakening of the two OHO hydrogen bonds by double deuteration [1]. This effect is absent in the weaker NHN hydrogen

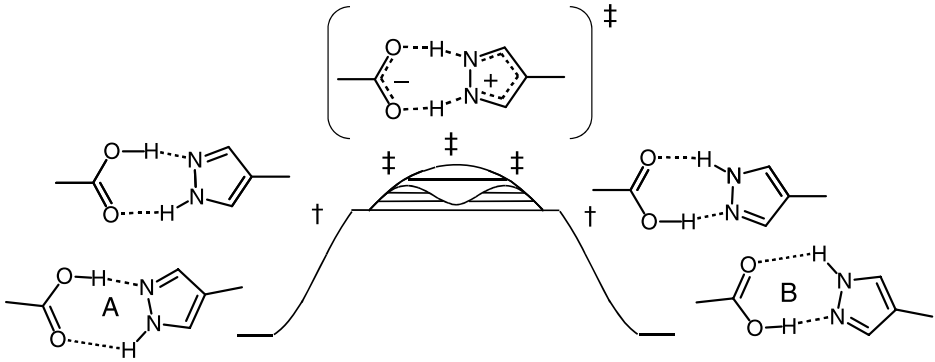

Fig. 15. Visualization of small angle reorientation during the concerted or stepwise double proton transfer between two hydrogen bonded molecules of PCA.

bonds of DPBrP where E_m is larger than for benzoic acid dimer. Such a large value has been associated with a substantial heavy atom motion arising from hydrogen bond compression in order to reach the pre-tunneling state [1,3].

The finding that in the case of PCA E_m is larger and the kinetic isotope effects much smaller than in benzoic acid dimer and DPBrP is consistent with an even larger heavy atom motion before the pre-tunneling state is reached as illustrated in Fig. 15. The data do not allow us to distinguish between a stepwise and a concerted motion, but as mentioned above, both cases merge in the case of small barriers. We speculate that the heavy atom motion is associated with a small angle rotation of the two reacting PCA molecules by which especially the O···H–N hydrogen bond is strengthened, leading to a collinear arrangement. One might argue that such a motion should not require much more energy than the hydrogen bond compression in DPBrP. However, such a compression will not be hindered by adjacent molecules as in the case of PCA where the double proton transfer in a given double hydrogen bond unit may be influenced by the tautomeric state of an adjacent hydrogen bond unit.

4.3 The mechanism of proton transfer through the hydrogen bonded ribbons of PCA

The above-mentioned coupling of the double proton transfer with small angle rotations of PCA molecules and the corresponding molecular motions of PCA ribbons, lead to a mechanism of the proton tautomerism and order-disorder transition visualized schematically in Fig. 16. At low temperatures, a given ribbon adopts an all-syn conformation ...ABABA... (see Fig. 3a). Upon temperature increase, a double proton transfer in a given unit will lead to a double defect of the type ..ABBBA.. of higher energy but also of higher entropy as compared to the initial state. This defect will then separate and dissociate into two single defects which move along the ribbon. It is difficult to estimate whether these reaction steps are downhill or uphill in free enthalpy. We assign the main mechanism of double proton transfer in solid PCA to the propagation of single defects through the ribbon as illustrated in the last step, consisting of the interconversion steps

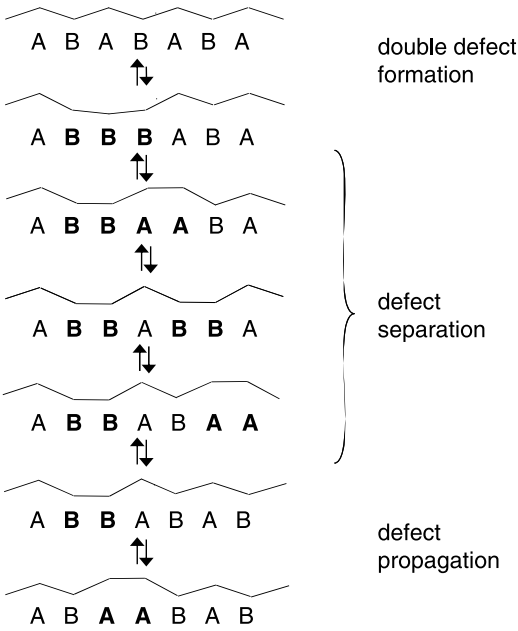

Fig. 16. Proposed mechanism for the order-disorder transition and of degenerate double proton transfer in solid PCA. At low temperatures, the undulated curved ribbon with localized or ordered protons is realized. When temperature is increased, a non-degenerate double proton transfer produces a double defect. The double defect separates into two single defects. After separation, a single defect propagates *via* a degenerate double proton transfer along the ribbon, producing proton disorder.

between AA and BB. Of all steps in Fig. 16, this step is the one whose equilibrium constant is closest to unity, *i.e.* it represents a quasi-degenerate step. Only an ideal ribbon of infinite length will exhibit an ideal order-disorder transition in a given temperature range. A distribution of finite chain lengths, or other chain imperfections, will change the order-disorder transition temperature of a given ribbon which explains that different PCA samples may exhibit slightly different and broad transition temperatures. To our knowledge, this kind of transition constitutes a case which has not yet observed before.

We note that this mechanism is similar to the one of proton exchange in pure protic solvents such as methanol (AH) [55]. Here, in the first step the dissociation into the solvated cation AH_2^+ and the anion A^- takes place – which requires energy but increases entropy, then the two ions separate, and eventually both ions move independently through the liquid via proton transfer to and from AH.

5. Conclusions

Using a combination of longitudinal ^{15}N and ^{2}H relaxometry, we have obtained rate constants of the double HH, HD and DD transfers in solid dimeric units of PCA ribbons (Fig. 2). Within the margin of error, no kinetic isotope effects (KIE) were observed. This is unusual as compared to pyrazole dimers and benzoic acid dimers, which exhibit

large kinetic HH/HD/DD isotope effects. We associate the absence of KIE in PCA to small molecular reorientations preceding proton tunneling and during proton tunneling. A mechanism for the observed order-disorder transition of PCA is proposed.

Acknowledgement

We thank the Deutsche Forschungsgemeinschaft, Bonn for financial support.

References

1. H. H. Limbach, Single and Multiple Hydrogen/Deuterium Transfer Reactions in Liquids and Solids, in: *Hydrogen Transfer Reactions*, J. T. Hynes, J. Klinman, H. H. Limbach, R. L. Schowen (Eds.), Wiley-VCH, Weinheim (2007), Chapt. 6, p. 135–221.
2. H. H. Limbach, J. M. Lopez, and A. Kohen, Philos. Trans. B (London) **361** (2006) 1399.
3. H. H. Limbach, K. B. Schowen, and R. L. Schowen, J. Phys. Org. Chem. **23** (2010) 586.
4. Z. Smedarchina, W. Siebrand, A. Fernandez-Ramos, Multiple Proton Transfer: From Stepwise to Concerted, in: *Hydrogen Transfer Reactions*, J. T. Hynes, J. Klinman, H. H. Limbach, R. L. Schowen (Eds.), Wiley-VCH, Weinheim (2007), Chapt. 29, p. 895–945.
5. Z. Smedarchina, W. Siebrand, A. Fernandez-Ramos, and R. Meana-Paneda, Z. Phys. Chem. **222** (2008) 1291.
6. H. H. Limbach, O. Klein, J. M. Lopez Del Amo, and J. Elguero, Z. Phys. Chem. **217** (2004) 17.
7. H. H. Limbach, B. Wehrle, H. Zimmermann, R. D. Kendrick, and C. S. Yannoni, Angew. Chem. Int. Ed. Engl. **26** (1987) 247.
8. M. Schlabach, B. Wehrle, H. Rumpel, J. Braun, G. Scherer, and H. H. Limbach, Ber. Bunsenges. Phys. Chem. **96** (1992) 821.
9. B. H. Meier, F. Graf, and R. R. Ernst, J. Chem. Phys. **76** (1982) 767.
10. A. Stöckli, B. H. Meier, R. Kreis, R. Meyer, and R. R. Ernst, J. Chem. Phys. **93** (1990) 1502.
11. C. G. Hoelger, B. Wehrle, H. Benedict, and H. H. Limbach, J. Phys. Chem. **98** (1994) 843.
12. R. Hentschel and H. W. Spiess, J. Magn. Reson. **35** (1979) 157.
13. A. Heuer and U. Haeberlen, J. Chem. Phys. **95** (1991) 4201.
14. J. L. Skinner and H. P. Trommsdorff, J. Chem. Phys. **89** (1988) 897.
15. R. Meyer and R. R. Ernst, J. Chem. Phys. **93** (1990) 5518.
16. A. J. Horsewill, A. Heideman, and S. Hayashi, Z. Phys. B **90** (1993) 319.
17. Q. A. Xue, A. J. Horsewill, M. R. Johnson, and H. P. Trommsdorff, J. Chem. Phys. **120** (2004) 11107.
18. U. Langer, L. Latanowicz, C. Hoelger, G. Buntkowsky, H. M. Vieth, and H. H. Limbach, Phys. Chem. Chem. Phys. **3** (2001) 1446.
19. J. M. López del Amo, U. Langer, V. Torres, G. Buntkowsky, H. M. Vieth, M. Pérez-Torralba, D. Sanz, R. M. Claramunt, J. Elguero, and H. H. Limbach, J. Am. Chem. Soc. **130** (2008) 8620.
20. J. M. López del Amo, U. Langer, V. Torres, M. Pietrzak, G. Buntkowsky, H. M. Vieth, M. F. Shibl, O. Kühn, M. Bröring, and H.-H. Limbach, J. Phys. Chem. A **113** (2009) 2193.
21. R. Anulewicz, I. Wawer, T. M. Krygowski, F. Männle, and H. H. Limbach, J. Am. Chem. Soc. **119** (1997) 12223.
22. J. M. Lopez, F. Männle, I. Wawer, G. Buntkowsky, and H. H. Limbach, Phys. Chem. Chem. Phys. **9** (2007) 4498.
23. J. A. S. Smith, B. Wehrle, F. Aguilar-Parrilla, H. H. Limbach, M. C. Foces-Foces, F. H. Cano, J. Elguero, A. Baldy, M. Pierrot, M. M. T. Khurshid, and J. B. Larcombe-McDouall, J. Am. Chem. Soc. **111** (1989) 7304.
24. F. Aguilar-Parrilla, G. Scherer. H. H. Limbach, M. C. Foces-Foces, F. H. Cano, J. A. S. Smith, C. Toiron, and J. Elguero, J. Am. Chem. Soc. **114** (1992) 9657.

25. F. Toda, K. Tanaka, C. Foces-Foces, A. L. Llamas-Saiz, H. H. Limbach, F. Aguilar-Parrilla, R. M. Claramunt, C. Lopez, and J. Elguero, J. Chem. Soc. Chem. Comm. (1993) 1139.
26. F. Aguilar-Parrilla, H. H. Limbach, C. Foces-Foces, F. H. Cano, N. Jagerovic, and J. Elguero, J. Org. Chem. **60** (1995) 1965.
27. C. G. Hoelger, H. H. Limbach, F. Aguilar-Parrilla, J. Elguéro, O. Weintraub, and S. Vega, J. Magn. Reson. A **120** (1996) 46.
28. J. L. G. de Paz, J. Elguero, C. Foces-Foces, A. L. Llamas-Saiz, F. Aguilar-Parrilla, O. Klein, and H. H. Limbach, J. Chem. Soc. Perkin **2** (1997) 101.
29. F. Aguilar-Parrilla, O. Klein, J. Elguero, and H. H. Limbach, Ber. Bunsenges. Phys. Chem. **101** (1997) 889.
30. O. Klein, M. M. Bonvehi, F. Aguilar-Parrilla, J. Elguero, and H. H. Limbach, Isr. J. Chem. **34** (1999) 291.
31. O. Klein, F. Aguilar-Parrilla, J. M. López del Amo, N. Jagerovic, J. Elguero, and H. H. Limbach, J. Am. Chem. Soc. **126** (2004) 11718.
32. R. L. Redington, T. E. Redington, and R. L. Sams, Z. Phys. Chem. **222** (2008) 1197.
33. J. J. Titman, Z. Luz, and H. W. Spiess, J. Am. Chem. Soc. **114** (1992) 3756.
34. N. M. Szeverenyi, A. Bax, and G. E. Maciel, J. Am. Chem. Soc. **105** (1983) 2579.
35. C. Foces-Foces, A. Echevarría, N. Jagerovic, I. Alkorta, J. Elguero, U. Langer, O. Klein, M. Minguet-Bonvehí, and H. H. Limbach, J. Am. Chem. Soc. **123** (2001) 7898.
36. R. M. Claramunt, M. A. García, and C. López, J. Elguero, Arkivoc **vii** (2005) 91.
37. J. Elguero and R. Jacquier, Bull. Soc. Chim. Fr. (1966) 2832.
38. R. Hüttel, F. Büchele, and P. Jochum, Chem. Ber. **88** (1955) 1577.
39. B. Bak, C. H. Christensen, D. Christensen, T. S. Hansen, E. J. Pedersen, and J. T. Nielsen, Acta Chem. Scand. **19** (1965) 2434.
40. P. J. Du Bois Murphy, J. Magn. Reson. **70** (1986) 307.
41. D. Torchia, J. Magn. Reson. **30** (1978) 613.
42. R. D. Kendrick, S. Friedrich, B. Wehrle, H. H. Limbach, and C. S. Yannoni, J. Magn. Reson. **65** (1985) 159.
43. B. Wehrle, F. Aguilar-Parrilla, and H. H. Limbach, J. Magn. Reson. **87** (1990) 584.
44. E. R. Andrew and L. Latanowicz, J. Magn. Reson. **68** (1986) 232.
45. H. H. Limbach, M. Pietrzak, S. Sharif, P. M. Tolstoy, I. G. Shenderovich, S. N. Smirnov, N. S. Golubev, and G. S. Denisov, Chem. Eur. J. **10** (2004) 5195.
46. B. C. K. Ip, I. G. Shenderovich, P. M. Tolstoy, J. Frydel, G. S. Denisov, G. Buntkowsky, and H. H. Limbach, J. Phys. Chem. A **116** (2012) XXXX-XXXX (DOI: 10.1021/jp305863n).
47. R. J. Wittebort, M. G. Usha, D. J. Ruben, D. E. Wemmer, and A. Pines, J. Am. Chem. Soc. **110** (1988) 5668.
48. B. Walaszek, Y. Xu, A. Adamczyk, H. Breitzke, K. Pelzer, H. H. Limbach, J. Huang, H. Li, and G. Buntkowsky, Solid State Nucl. Magn. Reson. **35** (2009) 164.
49. J. A. Jiménez, R. M. Claramunt, O. Mó, F. Wehrmann, G. Buntkowsky, H. H. Limbach, R. Goddard, and J. Elguero, Phys. Chem. Chem. Phys. **1** (1999) 5113.
50. W. R. Medycki, E. C. Reynhardt, and L. Latanowicz, Mol. Phys. **93** (1998) 323.
51. J. Schmidt and D. Sebastiani, J. Chem. Phys. **123** (2005) 074501.
52. M. Schlabach, B. Wehrle, H. Rumpel, J. Braun, G. Scherer, and H. H. Limbach, Ber. Bunsenges. Phys. Chem. **96** (1992) 821.
53. S. Schweiger and G. Rauhut, J. Phys. Chem. A **107** (2003) 9668.
54. M. Schlabach, H. H. Limbach, E. Bunnenberg, A. Shu, B. R. Tolf, and C. Djerassi, J. Am. Chem. Soc. **115** (1993) 4554.
55. D. Gerritzen and H. H. Limbach, Ber. Bunsenges. Phys. Chem. **85** (1981) 527.